




Article

Low-Temperature Annealing of Nanoscale Defects in Polycrystalline Graphite

Gongyuan Liu ^{1,†}, Hajin Oh ^{1,†}, Md Hafijur Rahman ¹, Jing Du ¹, William Windes ² and Aman Haque ^{1,*} 

¹ Department of Mechanical Engineering, The Pennsylvania State University, University Park, PA 16803, USA; gxl5293@psu.edu (G.L.); oh339@psu.edu (H.O.); mxr5923@psu.edu (M.H.R.); jingdu@psu.edu (J.D.)

² Idaho National Laboratory, Idaho Falls, ID 83415, USA; william.windes@inl.gov

* Correspondence: mah37@psu.edu

† These authors contributed equally to this work.

Abstract: Polycrystalline graphite contains multi-scale defects, which are difficult to anneal thermally because of the extremely high temperatures involved in the manufacturing process. In this study, we demonstrate annealing of nuclear graphite NBG-18 at temperatures below 28 °C, exploiting the electron wind force, a non-thermal stimulus. High current density pulses were passed through the specimens with a very low-duty cycle so that the electron momentum could mobilize the defects without heating the specimen. The effectiveness of this technique is presented with a significant decrease in electrical resistivity, defect counts from X-ray computed tomography, Raman spectroscopy, and nanoindentation-based mechanical characterization. Such multi-modal evidence highlights the feasibility of nanoscale defect control at temperatures about two orders of magnitude below the graphitization temperature.

Keywords: polycrystalline graphite; non-thermal annealing; electron wind force; Raman spectroscopy



Citation: Liu, G.; Oh, H.; Rahman, M.H.; Du, J.; Windes, W.; Haque, A. Low-Temperature Annealing of Nanoscale Defects in Polycrystalline Graphite. *C* **2024**, *10*, 76. <https://doi.org/10.3390/c10030076>

Academic Editor: Cédric Pardanaud

Received: 3 July 2024

Revised: 14 August 2024

Accepted: 23 August 2024

Published: 26 August 2024



Copyright: © 2024 by the authors. Licensee MDPI, Basel, Switzerland. This article is an open access article distributed under the terms and conditions of the Creative Commons Attribution (CC BY) license (<https://creativecommons.org/licenses/by/4.0/>).

1. Introduction

Graphite is one of the highest-impact technology materials with structural (neutron moderator in nuclear reactors) and electrode (batteries, sensors, catalysis) applications [1]. Polycrystalline graphite is a hierarchical material consisting of grains, which in turn consist of crystallite units of parallel stacking of carbon hexagonal layers [2]. Their exceptional stability under high temperatures, radiation, and chemically aggressive conditions makes them attractive for harsh environment technologies. One major example is the nuclear sector; polycrystalline graphite is widely used as the moderator, reflector, and core support structures in nuclear reactors because of their excellent resistance to radiation and high operating temperatures [3,4]. Harsh manufacturing processes lead to defects spanning atomic [5] to sub-millimeter scales [6,7], contributing to up to 20% of the overall volume of the material [8,9]. Further proliferation of defects can take place inside a nuclear reactor due to the high temperature, radiation, and structural loads. For example, neutron irradiation generates a large number of interstitial and vacancy point defects [10] that agglomerate and collapse into dislocation loops [11]. Dimensional changes take place with initial shrinkage of the nanoscale Mrozowski cracks followed by the formation of additional planes in the c-axis [12]. Chemical degradation also takes place via thermal oxidation [13,14]. All these microstructural changes may lead to dramatic deterioration of mechanical and thermal properties [15].

Since graphite is processed at temperatures up to 2300–2800 °C, the pre-existing defects are difficult to mitigate by conventional thermal post-manufacturing annealing [16–18]. The extent of annealing may depend on the grain size, irradiation temperature, and accumulated neutron dose [19]. The interstitials can move freely in any direction perpendicular or parallel to the base planes. Their annealing activation energy and temperature are lower compared to vacancies, which can move only along the planes at higher temperatures.

Large loops of interstitial atoms and vacancies would require a higher temperature range. The basic physics of thermal annealing involves random diffusional motion of the defect due to atomic vibration. Therefore, the process is also time-consuming. In addition, too high a temperature may introduce fullerene-like defects due to the migration of basal-plane defects, leading to non-recoverable dimensional changes due to swelling [20].

In this study, we investigate the electron wind force (EWF) as a non-thermal stimulus for graphite annealing. The EWF is an atomic scale mechanical force developed by defect–electron interaction due to the passage of electrical current through conducting or semiconducting materials. Whenever the electrons collide with a defect, they lose their momentum. This momentum transfer applies a mechanical force on the defect. Typically, Joule heating overshadows the EWF to cause thermal runaway, known as the electromigration damage [21]. We argue that if we are able to suppress the Joule heating, the EWF may have benign effects on the defect mobility. The literature suggests that it can overcome the activation barrier to influence defect density, grain size, and phases in metallic materials [22]. In this study, we eliminate Joule heating by passing high-density electrical current pulses with a very low-duty cycle through the specimen. The low-duty cycle suppresses any rise in the average specimen temperature. A similar approach, albeit allowing high temperature, has resulted in transformations in intermetallic compound formation, growth in diffusion couples, precipitation, crystallization of amorphous alloys, and recrystallization and grain growth of cold-worked metals [23]. However, there is no evidence of low-temperature annealing of graphite in the literature, which motivates this study.

2. Materials and Methods

We performed low-temperature annealing of as-received polycrystalline graphite using the EWF arising from microsecond pulses of electrical current. The effectiveness of the proposed technique is presented through multiple modalities such as (i) a decrease in electrical resistivity, (ii) X-ray computed tomography, (iii) nanopore size distribution from scanning electron microscopy, (iv) Raman spectroscopy, and (v) static and dynamic mechanical testing. The annealing experimental setup is shown in Figure 1a. Electrical resistance measurement, nano X-ray computed tomography (nano-XCT), scanning electron microscopy (SEM), Raman spectroscopy, and Nanoindentation were also conducted. Details of these methods are provided below.

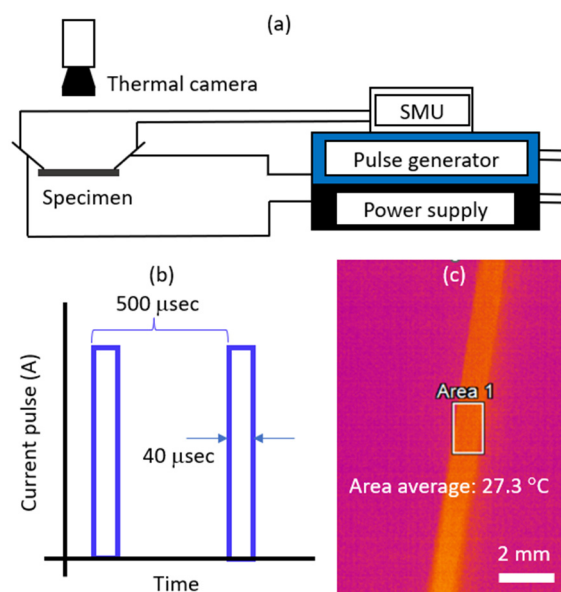


Figure 1. (a) Schematic diagram of the experimental setup. (b) Time vs. current graph of the electrical pulses. (c) Infrared image of a specimen during electron wind force annealing.

Specimen material and preparation: This study involves NBG-18 (SGL Carbon Group, Wiesbaden, Germany) nuclear graphite. This choice is motivated by the unique heterogeneity of the defects and microstructure of the material, which makes it a favorable specimen for any basic research on annealing. Defects in nuclear graphite strongly influence mechanical and thermal properties, highlighting the technological significance of reactor operation and safety. NBG-18 is pitch-coke-based, vibrationally molded graphite as specimen material. Ten specimens were sectioned into rectangular bars ($1 \times 1 \times 25 \text{ mm}^3$) and polished with diamond paste with particles ranging from 14 to 0.25 microns. The polished specimens had cross-sections of approximately $0.75 \times 0.75 \text{ mm}^2$.

Low-temperature EWF annealing: Current pulses at ambient pressure were applied to the specimens by integrating a DC Power supply (DCS 100-12E, Sorensen, San Diego, CA, USA) with a pulse generator (eDrive, Northrop Grumman, Falls Church, VA, USA). An infrared camera (PI-640, Optris, Berlin, Germany) was utilized to monitor the sample temperature during electropulsing. The specimens were annealed for 2 min (240 pulses) each, with simultaneous measurement of electrical resistivity. Out of 240 pulses, most of the resistivity decrease took place in the first few pulses. During the annealing, we monitored the specimen temperature with an infrared microscope. Current density was varied from 25 to 45 A/mm², with 40 micro-second current pulses at 2 Hz frequency. This is shown in Figure 1b. The very short pulse duration and the long time between pulses (498 microseconds) dissipated the Joule heat. The resulting temperature profile was triangular in nature, ranging from 21 °C at the base to 42 °C at the peak. The average temperature during the annealing process ranged between 28 and 30 °C, as shown in Figure 1c.

Monitoring of Electrical Resistance: The resistance of the samples was monitored using a 2-channel source measure unit (2636B, Keithley, Cleveland, OH, USA). The pre-annealing resistance was measured before the electropulsing treatment. Kelvin clips were used to perform 4-point probing to avoid the influence of any contact resistance. The current density was calculated by dividing a passed current by the cross-sectional area of the samples. The resistivity at each stage of current density was compared with the initial value, and the percentage changes were calculated.

Nano X-ray CT and Raman Spectroscopy: Micro-CT imaging of the samples was performed at the laboratory-based micro-CT (Xradia 620 Versa, ZEISS, Oberkochen, Germany). A cylindrical volume of 0.73 mm \times 0.75 mm (d \times H) was selected as the region of interest. Micro-CT scan was then carried out using a voltage of 80 kV and an X-ray source of 10 W. An isometric voxel size of 0.38 μm was achieved. The tomographic images were imported into Avizo 2022.1 software (FEI Visualization Sciences Group, Burlington, MA, USA) for image processing and analysis. The micro-CT image stacks were segmented into graphite material and defects using Avizo. The image intensity threshold method was applied to distinguish the two phases mentioned above. The specimens' porosity was determined, and the sizes of defects were assessed by calculating their equivalent diameters. Subsequently, the histograms of the pulsed and pristine samples were compared. The Raman spectra of the samples were obtained using a Raman microscope (LabRAM Soleil, HORIBA, Osaka, Japan) equipped with a 50 \times microscopic objective lens. A typical setting of a 532 nm green laser with an incident power of 4 mW and an 1800 gr/mm grating was used.

Nanoindentation Testing: To understand the changes in mechanical properties of the samples after the electron wind force annealing, both as-received and annealed samples were subjected to static (0.2 s hold time) and dynamic (1000 s) nanoindentation. The nanomechanical test system (Hysitron TI 980, Bruker, Billerica, MA, USA) allowed indentation with Berkovich tip, loading up to 12.5 mN on graphite. For the accuracy of the data, the indentation process was conducted in different peak loads ranging from 5 mN to 12.5 mN to find the load that allows the minimum standard deviation. According to the experiment, 12.5 mN allowed a standard deviation lower than 0.15 GPa in average hardness, which was selected as the testing load. The examinations were conducted with nine points of indentations, formatting a 3 \times 3 array. The load time for each indentation was 0.5 s and the hold time was 0.2 s. This is useful to mitigate the nature of localized

probing during nanoindentation tests. The loads and displacement data were achieved from the native software to the nanoindenter equipment. Creep tests were performed by applying a 12.5 mN load in 0.5 s and then holding the load constant for 1000 s.

3. Results

The electrical resistivity of the specimens was monitored as an indirect measure of the effectiveness of the annealing process. Figure 2 shows a representative set of results for one specimen. The initial resistivity of $9.77 \mu\Omega\text{-m}$ remained almost constant as the current density was increased incrementally. At the current density of 25.2 A/mm^2 , the resistance dropped dramatically to 31.7% of the initial resistivity in less than 5 pulses. Continued pulsing did not decrease the resistivity further, indicating non-thermal annealing behavior. This is because the sluggish dynamics of thermal diffusion make time duration important only for thermal annealing. It became increasingly difficult to mobilize the remaining defects because the resistance decreased by only 2.2% when the current density was increased up to 44.5 A/mm^2 . This is because of the difference in mobilization or activation energies for the types of pre-existing or irradiation-induced defects. For example, the estimated activation energy for irradiated graphite increases from 1.1 eV to 8.9 eV as the defect morphology changes from mono to di vacancy [24]. For this study, the current density probably needed to be significantly increased to achieve the next level of defect annealing. We note that current density is the limitation of the present equipment; however, with a more sophisticated pulse generator, the resistance may further be reduced at higher current density. Interestingly similar magnitude of resistivity reduction was observed in the literature but at about $700 \text{ }^\circ\text{C}$ temperature [25].

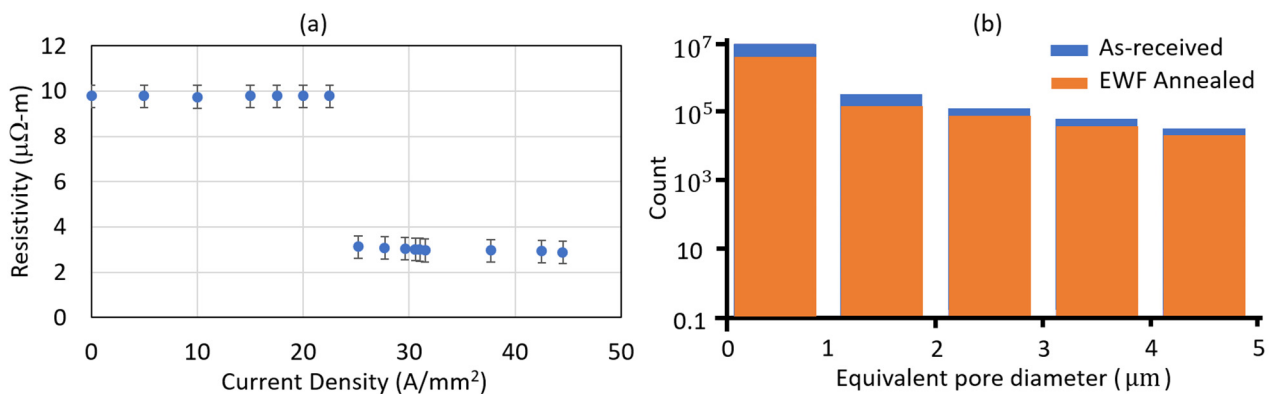


Figure 2. (a) Electrical resistivity of polycrystalline graphite NBG-18 as a function of electrical current density. (b) Equivalent diameter ($<5 \mu\text{m}$ range) of defects before and after the electron wind force annealing.

For more direct evidence of annealing, we measured the pore size distribution in the specimens before and after annealing. The first set of measurements was conducted using a Zeiss Xradia 620 Versa nano X-ray computed tomography scanner with 490 nm spatial resolution. Since the electron wind force is not expected to influence micro-scale and larger pores, the distributions of the defects with equivalent diameters $> 5 \mu\text{m}$ are excluded in Figure 2b. Interestingly, the results indicate a small decrease in the number count of these defects, which could be due to the collapsing of the pores due to the collective motion of the nanoscale defects. Since nanoscale pores could not be detected by the X-ray CT, we obtained 6 scanning electron microscope (SEM) images for each specimen before and after annealing and these were processed for pattern recognition (with the ImageJ 1.54c software) to detect submicron scale changes. Details of the surface pore analysis are provided as Supplementary Information. The pore size ranges from 0.1 to 3 microns in these specimens. However, it is important to note that this is not the pore range for the bulk NBG-18, since the images were taken to avoid very large voids. Table 1 shows that the post-annealing

average defect size appreciably decreased in the submicron range. It is important to note that the image numbers in Table 1 do not correspond to the exact same location in the specimens before and after annealing. The surface pores did not follow any specific pattern over the large area. Therefore, we took six images on six different locations on each of the specimens to improve the data reliability. In this sample population, we see a general trend of a decrease in the total pore area after annealing. Also, the average pore area decreases from $0.0795 \mu\text{m}^2$ to $0.0145 \mu\text{m}^2$. To further improve the quality of this analysis, we could either increase the sample population or fix the analysis on a specific location in the sample and analyze the pores before and after annealing. The latter is very challenging because of the random feature surfaces of the graphite. We therefore adopted the former approach and took six image numbers after noticing the consistency of the decreasing pore area tendency in the data. Unfortunately, even after the most accurate analysis, the caveat remains that SEM-based analysis contains surface information only. However, it offers a critical insight into the very small defects that are elusive to the highest resolution of X-ray CT currently available.

Table 1. Average pore area for the graphite specimens before and after the electron wind force annealing (44.5 A/mm^2).

Pore Area before Annealing			
Image	# of Pores	Total Pore Area (μm^2)	Average Pore Area (μm^2)
1	690	28.101	0.041
2	1919	58.079	0.03
3	1982	210.01	0.106
4	1236	183.445	0.148
5	1262	127.346	0.101
6	2229	114.705	0.051
Pore Area after annealing			
Image	# of Pores	Total Pore Area (μm^2)	Average Pore Area (μm^2)
1	1980	19.455	0.01
2	761	14.007	0.018
3	1729	35.914	0.021
4	940	8.491	0.009
5	2609	37.451	0.014
6	4399	68.34	0.016

Raman spectroscopy is widely regarded as a reliable tool for assessing crystallinity and defect density in carbon materials. Figure 3 shows the average Raman spectra for specimens before and after annealing at $28 \text{ }^\circ\text{C}$ temperature and 44.5 A/mm^2 . The only time we observed appreciable change in Raman spectra was at 25.2 A/mm^2 , which corresponds well to the electrical resistivity data presented in Figure 2a. Since the material is not uniformly solid, for each specimen, nine spots were carefully chosen to avoid micro cracks or voids under the microscope to acquire the spectra. For graphite, the peaks around 1350 cm^{-1} , 1580 cm^{-1} , and 2720 cm^{-1} are known as D, G, and 2D bands, respectively [11]. The presence of disorder in sp^2 -hybridized carbon systems results in resonance Raman spectra; therefore, the intensity of the D band is directly proportional to the level of planar defects in the sample [11]. The as-received NBG-18 contains a D-band peak intensity of 127 at 1350 cm^{-1} , whereas the pulsed sample contains an intensity of 116 at 1347 cm^{-1} . In other words, the intensity of the defect-proportional peak decreased by 8.66%. The G peak comes

from the bond stretching of all pairs of sp^2 -hybridized atoms and hence reflects the order in the crystal. The G peak intensity increased from 144.5 to 244.8 (69.4% increase) after the electron wind force annealing. The average Raman intensity ratio (I_D/I_G) is 0.88 for the as-received specimens, which decreases to 0.47 after the electron wind force annealing. The ratio is proportional to the square root of the defect quantity [26] and is commonly used as an indicator of the defect density in carbon materials [27]. According to Tunistra and Koenig [28], the intensity ratio is inversely proportional to the in-plane crystallite size. Our results therefore indicate about 2-times growth in the characteristic crystallite size after annealing. Another evidence of the annealing effect is due to the 45% increase in the intensity of the 2D peak. This peak reflects a second order Raman mode generated by graphene layers without any kind of disorder or defects [29].

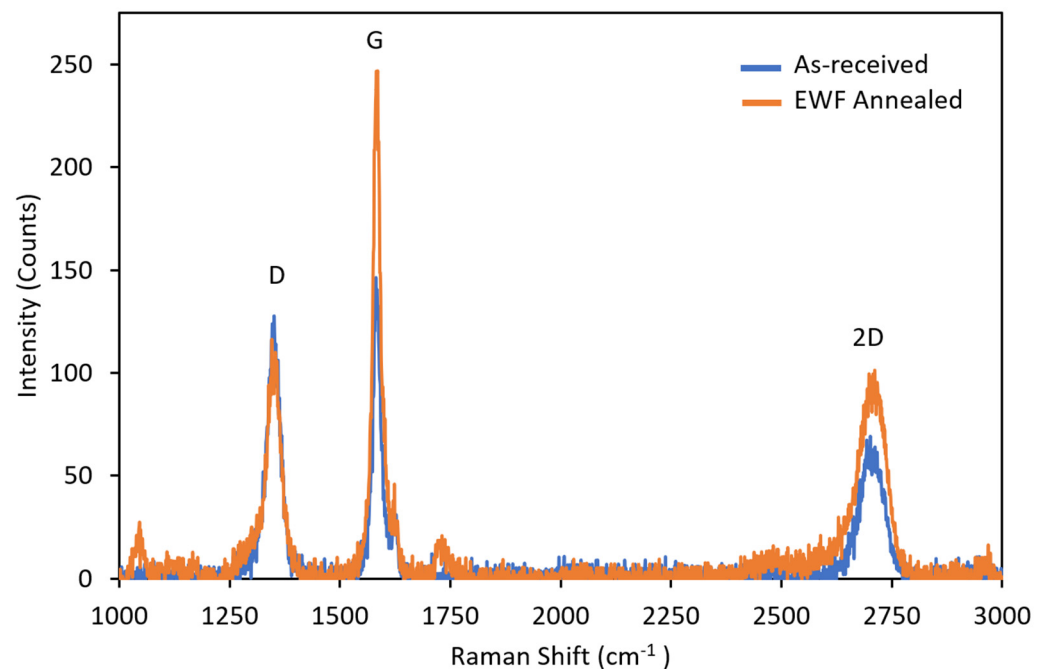


Figure 3. Average Raman spectra of NBG-18 as-received and electron wind force annealed at 28 °C temperature and 44.5 A/mm².

The final modality for the annealing effectiveness in this study is through the assessment of mechanical properties. It is expected that reduced defect density in post-anneal specimens will increase their elastic modulus and hardness. We therefore measured these properties by performing nanoindentation on nine spots on each of the fine-polished specimens. Figure 4a shows the average load-displacement curves for nine indentations spaced 10 μm equally to each other on each type of specimen. The average hardness of the pre-annealing graphite was 380 ± 24 MPa, whereas that of post-annealing graphite was 580 ± 18 MPa. The proposed electron wind force annealing therefore introduced a 52.63% increase in average hardness. The average reduced modulus of as-received and annealed specimens was 11.26 ± 0.54 GPa and 11.79 ± 0.45 GPa, respectively, which was a 4.7% difference in the average reduced modulus. Figure 4b shows the displacement-time curves for 10 mN indentation load. The remarkably smaller displacement in the annealed specimen agrees with the data with 0.2 s holding time. Since creep is known to increase with defects and porosity [30], the annealed specimen is expected to show better primary creep resistance compared to the as-received ones. The mechanical properties at different current densities closely followed the electrical resistivity (Figure 2a) and Raman spectra (Figure 3) data. The only time we observed appreciable change in average force-displacement data was at 25.2 A/mm², which corresponds well to the electrical resistivity data presented in Figure 2a.

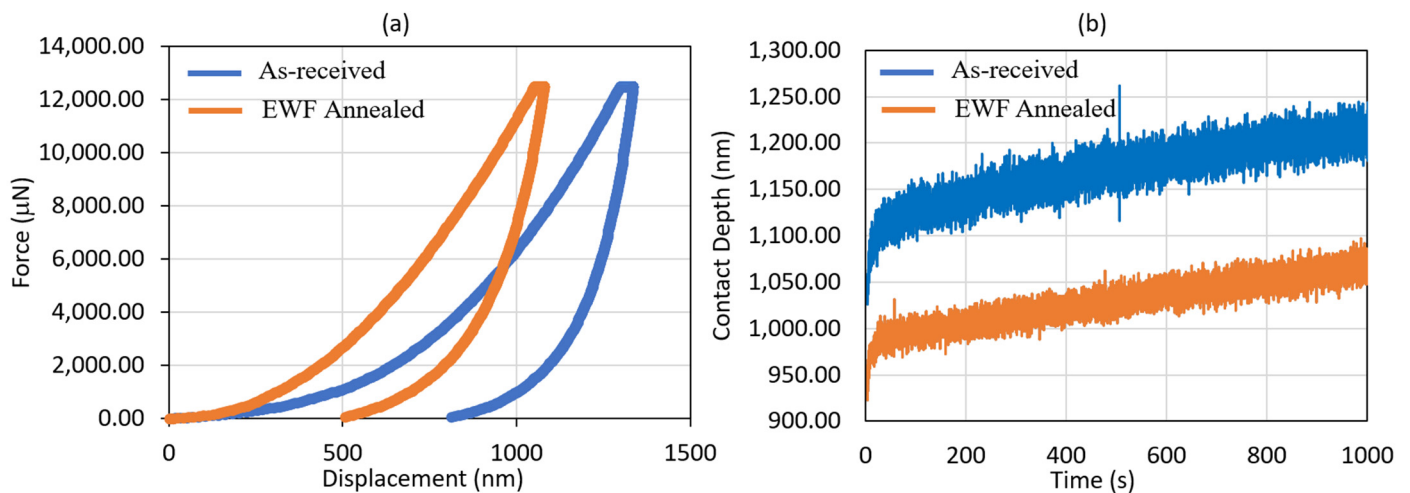


Figure 4. Nanoindentation tests on as-received NBG-18 nuclear graphite and annealed graphite at 28 °C temperature and 44.5 A/mm². (a) Average force–displacement curves with 0.2 s hold time. (b) Collective displacement–time data for all the specimens with 1000 s hold time.

4. Discussion

Annealing of defects is a very common activity in basic and applied materials' research and development. Thermal annealing is the only known way to anneal defects, where the origin of the heat can be from the laser, microwave, electrical current, or a furnace. The process parameters include temperature and time depending on the material type but in general, very high temperatures and longer times are needed. For example, the homologous temperature could be 0.5 or more. As a result, materials that undergo high-temperature processing are difficult to anneal. This is the biggest challenge for graphitic materials, which by default require graphitization temperature for effective annealing. This study shifts from that paradigm by mobilizing and annihilating defects using a non-thermal stimulus. This unique approach, in principle, does not need high temperatures, which is demonstrated in this study. The benefit is the energy efficiency of the approach originating from low power requirements. For example, a 100 A current pulse with 40 μs width takes 0.6 J energy for a graphite specimen with 1.5 Ω resistance. For a cycle time of 0.5 s, the average power is only 1.2 W. It is important to note that even though we applied the pulsed current for 2 min, most of the defects are annealed in the first few seconds. This is a major contrast between EWF and thermal annealing. Time duration is important for thermal annealing because the process is random, and defects take a long time to reach global energy minima.

A notable aspect of the EWF annealing is that it cannot modify or annihilate large defects, such as a 10-micron diameter pore. This is because the magnitude of the EWF is a small quantity. It is most effective on 2-dimensional defects, such as grain boundaries, and moderately efficient on 1- or 0-dimensions such as dislocations and vacancies/interstitial clusters. Figure 5 shows X-CT scans for the as-received and EWF-annealed specimens. Even at the highest resolution, the technique cannot show 0, 1, or 2 dimensional defects. At the same time, EWF does not have the activation energy to discernably influence pores and voids. For this reason, the conventional X-CT technique is not the best way to characterize the electrical wind force-based annealing effectiveness. Because the highest resolution is close to 1 micron in this study, our X-CT results needed to be analyzed only in the smaller defect sizes. SEM measurements may provide better resolution to highlight the annealing effects, but the outcome is from the surface only. Similarly, Raman spectroscopy is probably the most accurate and sensitive technique to study defects, but it too is a surface probing tool. It is therefore very important to prepare the specimen surface and probe only in the flat solid regions. A large number of data points were taken to balance these sources of error. We followed the same strategy for nanoindentation. Extra caution was taken because of the heterogeneity of the defect size and materials' crystallinity. In future, we plan to

measure bulk properties, which can capture the annealing effectiveness. This is already reflected in our electrical resistance characterization.

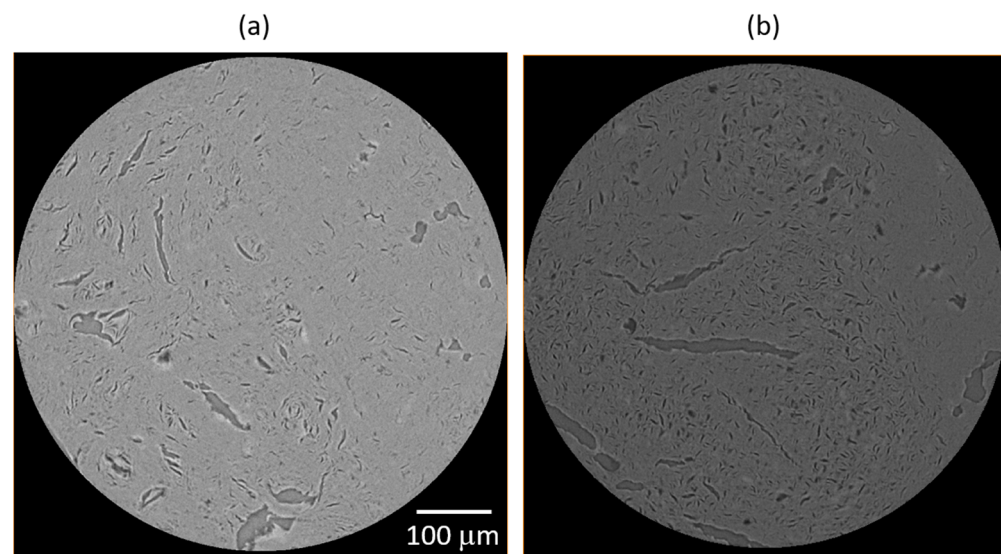


Figure 5. X-ray computed tomography scans of (a) as-received NBG-18 nuclear graphite and (b) annealed graphite at 28 °C temperature and 44.5 A/mm².

Future work could involve the annealing of irradiated graphite specimens. Relatively accessible specimens could come from ion irradiation, which is a proven surrogate of neutron irradiation. Ion irradiation can provide very high damage (displacement per atom) in a very short amount of specimen preparation time with the added benefit of no radioactivity. A better procedure to mimic the reactor environment could be to perform ion irradiation at higher (500–600 °C) temperatures. Similarly, the EWF annealing conditions could be changed for better optimization as well. In this study, we highlighted the evidence that high temperature is not essential for graphite annealing. However, efficient annealing protocols could take advantage of the potential EWF-temperature synergy [31]. It could be possible to perform optimal annealing with the combination of moderate temperature and moderate current density to outperform the present study where we used low temperature and high current density. It is also important to note that a too high current density at microsecond pulse width may adversely affect the crystallinity (or conversely defects) of graphite. This is because the EWF is a non-thermal stimulus, which is derived from the mechanical momentum of the electrons. Thus, it has a resemblance to mechanical impact loading. Impact loading at defect sites may lead to mobilization for energy levels higher than the activation energy of the type of defects. However, if very high energy loading is used, it may create new defects from the crystalline lattice, overshadowing the pre-existing defect mobilization. Another reason is the undesired thermal shock loading effect. If very high current density is used in very short (microsecond) pulses, the thermal loading rate can rise exponentially, catastrophically failing the specimens because of the thermal runaway. Therefore, optimization of current density and temperature could be essential before any applied research on EWF annealing.

5. Conclusions

This study presents multiple modes of experimental evidence of ultrafast low-temperature annealing of graphite using the electron wind force. The proposed process required a current density as small as 25 A/mm² to initiate the defect-annealing process. The effectiveness of the novel annealing process is presented with four distinct types of evidence:

- i. Electrical resistivity decreased dramatically (about 4×) within a few seconds of annealing, reflecting a decrease in nanoscale defects in the specimens;

- ii. Electron wind force is more effective on grain/phase boundaries, dislocations, vacancies, dislocations, and interstitials compared to pores and voids;
- iii. A decrease in the Raman D-band peak (8.666%) and an increase in the G (69.4%) and 2D peak intensity (45%) reflect the effectiveness of the annealing process. The characteristic crystallite size was doubled after annealing;
- iv. Hardness and primary creep resistance improved significantly after the annealing process, which agrees with the first three observations.

The limited literature available on low-temperature treatment on nuclear graphite implies that the findings of this study can offer potentially new insights into the microstructure–property relationship in the high-temperature material. Future studies on comprehensive characterization including higher current density and annealing temperature would generate useful information for materials scientists.

Supplementary Materials: The following supporting information can be downloaded at: <https://www.mdpi.com/article/10.3390/c10030076/s1>, Figure S1: Raman spectra acquired at current density range of 0–25.2 A/mm². Figure S2: Raman spectra acquired at current density range of 25.2–44.5 A/mm². Figure S3. Juxtaposition of load-displacement curves for current density 0–25.2 A/mm². Table S1: Average mechanical properties for different current density inputs.

Author Contributions: Conceptualization, A.H.; Formal analysis, G.L., H.O., M.H.R., J.D., W.W. and A.H.; Funding acquisition, A.H.; Investigation, G.L., H.O., M.H.R. and J.D.; Methodology, G.L., H.O., M.H.R., J.D. and A.H.; Project administration, A.H.; Resources, W.W. and A.H.; Validation, G.L.; Writing—original draft, G.L. and H.O.; Writing—review and editing, J.D., W.W. and A.H. All authors have read and agreed to the published version of the manuscript.

Funding: This work was funded by the U.S. Department of Energy through the Nuclear Energy University Program (DE-NE0009129). The content of the information does not necessarily reflect the position or the policy of the federal government, and no official endorsement should be inferred. Partial support from the US Army Research Office through award #W911NF-23-1-0359 is also acknowledged. The views expressed in the article do not necessarily represent the views of the U.S. DOE or the United States Government.

Data Availability Statement: The raw data supporting the conclusions of this article will be made available by the authors on request.

Conflicts of Interest: The authors declare no conflicts of interest. The funders had no role in the design of the study; in the collection, analyses, or interpretation of data; in the writing of the manuscript; or in the decision to publish the results.

References

1. Duan, S.-Z.; Wu, X.-W.; Wang, Y.-F.; Feng, J.; Hou, S.-Y.; Huang, Z.-H.; Shen, K.; Chen, Y.-X.; Liu, H.-B.; Kang, F.-Y. Recent progress in the research and development of natural graphite for use in thermal management, battery electrodes and the nuclear industry. *New Carbon Mater.* **2023**, *38*, 73–91. [\[CrossRef\]](#)
2. Inagaki, M. Applications of Polycrystalline Graphite. In *Graphite and Precursors*; Delhaes, P., Ed.; Gordon & Breach Science Publishers: London, UK, 2001; pp. 179–199.
3. Marsden, B.J.; Haverty, M.; Bodel, W.; Hall, G.; Jones, A.; Mummery, P.; Treifi, M. Dimensional change, irradiation creep and thermal/mechanical property changes in nuclear graphite. *Int. Mater. Rev.* **2016**, *61*, 155–182. [\[CrossRef\]](#)
4. Zhou, X.-W.; Tang, Y.-P.; Lu, Z.-M.; Zhang, J.; Liu, B. Nuclear graphite for high temperature gas-cooled reactors. *New Carbon Mater.* **2017**, *32*, 193–204. [\[CrossRef\]](#)
5. Gruber, J.; Barsoum, M.W.; Tucker, G.J. Characterization of ripplcation mobility in graphite. *Mater. Res. Lett.* **2020**, *8*, 82–87. [\[CrossRef\]](#)
6. Arregui-Mena, J.D.; Worth, R.N.; Bodel, W.; März, B.; Li, W.; Campbell, A.A.; Cakmak, E.; Gallego, N.; Contescu, C.; Edmondson, P.D. Multiscale characterization and comparison of historical and modern nuclear graphite grades. *Mater. Charact.* **2022**, *190*, 112047. [\[CrossRef\]](#)
7. Liu, D.; Flewitt, P.E.J. Deformation and fracture of carbonaceous materials using in situ micro-mechanical testing. *Carbon* **2017**, *114*, 261–274. [\[CrossRef\]](#)
8. Kane, J.; Karthik, C.; Butt, D.P.; Windes, W.E.; Ubic, R. Microstructural characterization and pore structure analysis of nuclear graphite. *J. Nucl. Mater.* **2011**, *415*, 189–197. [\[CrossRef\]](#)

9. Zhu, Y.; Huang, Q.; Li, C.; Xie, R.; Fu, Y.; Lei, Q.; Zhou, X. Pore Structure of Nuclear Graphite Obtained via Synchrotron Computed Tomography. *J. Nondestruct. Eval.* **2020**, *39*, 17. [[CrossRef](#)]
10. Karthik, C.; Kane, J.; Butt, D.P.; Windes, W.E.; Ubic, R. Neutron irradiation induced microstructural changes in NBG-18 and IG-110 nuclear graphites. *Carbon* **2015**, *86*, 124–131. [[CrossRef](#)]
11. Eapen, J.; Krishna, R.; Burchell, T.D.; Murty, K.L. Early Damage Mechanisms in Nuclear Grade Graphite under Irradiation. *Mater. Res. Lett.* **2014**, *2*, 43–50. [[CrossRef](#)]
12. Liu, D.; Cherns, D. Nano-cracks in a synthetic graphite composite for nuclear applications. *Philos. Mag.* **2018**, *98*, 1272–1283. [[CrossRef](#)]
13. Paul, R.M.; Contescu, C.I.; Gallego, N.C.; Smith, R.; Bass, J.; Kane, J.J.; Tzelepi, A.; Metcalfe, M. On the thermal oxidation of nuclear graphite relevant to high-temperature gas cooled reactors. *J. Nucl. Mater.* **2023**, *573*, 154103. [[CrossRef](#)]
14. Luo, X.; Robin, J.-C.; Yu, S. Comparison of Oxidation Behaviors of Different Grades of Nuclear Graphite. *Nucl. Sci. Eng.* **2005**, *151*, 121–127. [[CrossRef](#)]
15. Zhang, H.-Y.; Cheng, J.-X.; Song, J.-L.; Yin, H.-Q.; Tang, Z.-F.; Liu, Z.-J.; Liu, X.-D. Topography changes and microstructural evolution of nuclear graphite (IG-110) induced by Xe²⁶⁺ irradiation. *New Carbon Mater.* **2023**, *38*, 393–402. [[CrossRef](#)]
16. Burchell, T.D.; Pappano, P.J.; Strizak, J.P. A study of the annealing behavior of neutron irradiated graphite. *Carbon* **2011**, *49*, 3–10. [[CrossRef](#)]
17. Lv, S.; Gao, J.; Jin, Y.; Zhou, Z.; Zhao, Y.; Yano, T.; Li, Z. The structure evolution in neutron-irradiated nuclear graphite and post-annealing. *Radiat. Phys. Chem.* **2022**, *197*, 110156. [[CrossRef](#)]
18. Zhou, X.-W.; Zhang, K.-H.; Yang, Y.; Wang, L.; Zhang, J.; Lu, Z.-M.; Liu, B.; Tang, Y.-P. Properties and microstructures of a matrix graphite for fuel elements of pebble-bed reactors after hightemperature purification at different temperatures. *New Carbon Mater.* **2021**, *36*, 987–993. [[CrossRef](#)]
19. Maruyama, T.; Li, Z. Dimensional changes and thermal conductivity by annealing and its relation to the defect concentration and stored energy release of neutron-irradiated graphite. *J. Nucl. Sci. Technol.* **2019**, *56*, 1006–1013. [[CrossRef](#)]
20. Johns, S.; Yoder, T.; Chinnathambi, K.; Ubic, R.; Windes, W.E. Microstructural changes in nuclear graphite induced by thermal annealing. *Mater. Charact.* **2022**, *194*, 112423. [[CrossRef](#)]
21. Huntington, H.B. Electromigration in Metals. In *Diffusion in Solids*; Nowick, A.S., Burton, J.J., Eds.; Academic Press: Cambridge, MA, USA, 1975; pp. 303–352.
22. Liang, C.-L.; Lin, K.-L. The microstructure and property variations of metals induced by electric current treatment: A review. *Mater. Charact.* **2018**, *145*, 545–555. [[CrossRef](#)]
23. Lu, B.; Tang, K.; Wu, M.; Yang, Y.; Yang, G. Mechanism of Electropulsing Treatment Technology for Flow Stress of Metal Material: A Review. *Alloys* **2024**, *3*, 96–125. [[CrossRef](#)]
24. Latham, C.D.; Heggie, M.I.; Alatalo, M.; Öberg, S.; Briddon, P.R. The contribution made by lattice vacancies to the Wigner effect in radiation-damaged graphite. *J. Phys. Condens. Matter* **2013**, *25*, 135403. [[CrossRef](#)] [[PubMed](#)]
25. Paraskevoulakos, C.; Roebuck, B.; Hallam, K.R.; Flewitt, P.E.J. Temperature dependence of electrical resistivity, deformation, and fracture of polygranular graphite with different amounts of porosity. *SN Appl. Sci.* **2022**, *5*, 28. [[CrossRef](#)]
26. Lasithiotakis, M.; Marsden, B.J.; Marrow, T.J. Annealing of ion irradiation damage in nuclear graphite. *J. Nucl. Mater.* **2013**, *434*, 334–346. [[CrossRef](#)]
27. Ammar, M.R.; Galy, N.; Rouzaud, J.N.; Toulhoat, N.; Vaudey, C.E.; Simon, P.; Moncoffre, N. Characterizing various types of defects in nuclear graphite using Raman scattering: Heat treatment, ion irradiation and polishing. *Carbon* **2015**, *95*, 364–373. [[CrossRef](#)]
28. Tuinstra, F.; Koenig, J.L. Raman spectrum of graphite. *J. Chem. Phys.* **1970**, *53*, 1126–1130. [[CrossRef](#)]
29. Malard, L.M.; Pimenta, M.A.; Dresselhaus, G.; Dresselhaus, M.S. Raman spectroscopy in graphene. *Phys. Rep.* **2009**, *473*, 51–87. [[CrossRef](#)]
30. Langdon, T.G. Dependence of Creep Rate on Porosity. *J. Am. Ceram. Soc.* **1972**, *55*, 630–631. [[CrossRef](#)]
31. Rahman, M.H.; Todaro, S.; Waryoba, D.; Haque, A. Synergistic Thermal and Electron Wind Force-Assisted Annealing for Extremely High-Density Defect Mitigation. *Materials* **2024**, *17*, 3188. [[CrossRef](#)]

Disclaimer/Publisher’s Note: The statements, opinions and data contained in all publications are solely those of the individual author(s) and contributor(s) and not of MDPI and/or the editor(s). MDPI and/or the editor(s) disclaim responsibility for any injury to people or property resulting from any ideas, methods, instructions or products referred to in the content.